

PIS3R: Very Large Parallax Image Stitching via Deep 3D Reconstruction

Muhua Zhu^{1,2*}, Xinhao Jin^{1*}, Chengbo Wang^{1,2}, Yongcong Zhang^{1,2}, Yifei Xue^{1,2}, Tie Ji^{1,†},
Yizhen Lao^{1,†}

¹Hunan University ²DaHe.AI

{casmyzhu, jinxinhao, wangchb, yongcongzhang}@hnu.edu.cn, iflyhsueh@gmail.com, jietie_hnu@163.com,
yizhenlao@hnu.edu.cn

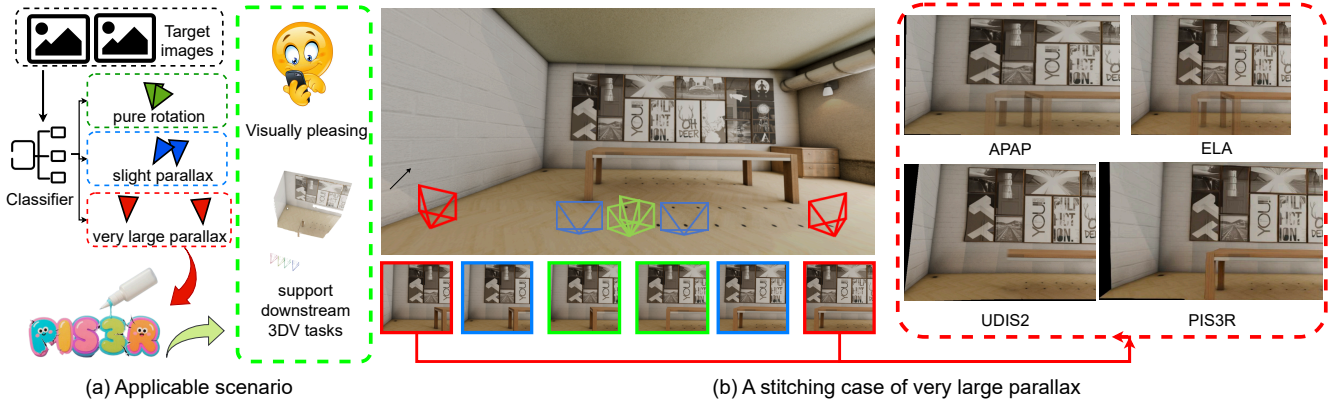


Figure 1: PIS3R for very large parallax image stitching. (a) The image stitching task can be classified (Sec. B in Appendix) into three cases based on the baseline between target images: *pure rotation*, *slight parallax*, and *very large parallax*. In this paper, we propose a novel image stitching solution named PIS3R, specifically for stitching images with *very large parallax*. (b) Representative existing image stitching methods (Zaragoza et al. 2014; Li et al. 2018; Nie et al. 2023) are unable to handle stitching tasks involving *very large parallax*. Instead, our solution is achieving promising results in such challenging scenario.

Abstract

Image stitching aim to align two images taken from different viewpoints into one seamless, wider image. However, when the 3D scene contains depth variations and the camera baseline is significant, noticeable parallax occurs—meaning the relative positions of scene elements differ substantially between views. Most existing stitching methods struggle to handle such images with large parallax effectively. To address this challenge, in this paper, we propose an image stitching solution called **PIS3R** that is robust to very large parallax based on the novel concept of deep 3D reconstruction. First, we apply visual geometry grounded transformer to two input images with very large parallax to obtain both intrinsic and extrinsic parameters, as well as the dense 3D scene reconstruction. Subsequently, we reproject reconstructed dense point cloud onto a designated reference view using the recovered camera parameters, achieving pixel-wise alignment and generating an initial stitched image. Finally, to further address potential artifacts such as holes or noise in the initial stitching, we propose a point-conditioned image diffusion module to obtain the refined result. Compared with existing methods,

our solution is very large parallax tolerant and also provides results that fully preserve the geometric integrity of all pixels in the 3D photogrammetric context, enabling direct applicability to downstream 3D vision tasks such as SfM. Experimental results demonstrate that the proposed algorithm provides accurate stitching results for images with very large parallax, and outperforms the existing methods qualitatively and quantitatively.

1 Introduction

Image stitching is a useful technique used to generate a wide field-of-view (FoV) scene by combining multiple images captured with limited FoV. It plays a vital role across various domains, including autonomous driving, medical imaging, surveillance, and virtual reality.

Most image stitching approaches follow a standard pipeline that begins by detecting and matching feature points among the input image pair. Based on these matches, global parametric transformations—typically homographies—are estimated to warp one image onto the coordinate system of the other. The final stitched result is then obtained by blending the warped image with the reference image, particularly resolving pixel values in overlapping regions.

* Equal contribution.

† Corresponding author: yizhenlao@hnu.edu.cn

Project page: <https://github.com/zmhcasmypis3r>

Image warping is a key challenge in image stitching. Homography, a widely used planar transformation model, assumes a flat scene (Hartley and Zisserman 2003). However, in real-world scenes with depth variation and large camera baselines, this assumption fails, leading to parallax effects and noticeable misalignments—especially near object boundaries.

1.1 Motivations

Very large parallax. To mitigate parallax artifacts in image stitching, adaptive warping methods have been developed that divide images into grids or pixels and apply locally varying transformations (Gao, Kim, and Brown 2011; Lee and Sim 2018; Li et al. 2018; Lin et al. 2011; Zaragoza et al. 2014; Zhang et al. 2016). Energy minimization frameworks further optimize these warps to reduce geometric distortion (Li et al. 2018; Lin et al. 2011; Zhang et al. 2016). Some approaches employ seam-cutting techniques to align local regions and conceal misalignments in others (Gao et al. 2013; Lin et al. 2016; Zhang and Liu 2014). However, existing smooth warping methods (Gao, Kim, and Brown 2011; Li et al. 2018; Lin et al. 2011; Zaragoza et al. 2014; Zhang et al. 2016) often fail under very large parallax, where adjacent pixels in one image may not correspond to nearby pixels in the other view. While video-based methods using epipolar geometry have been proposed (Lee and Sim 2018), they rely on temporal motion cues and are not directly applicable to still image stitching.

Downstream 3DV tasks. Almost all existing image stitching methods, including adaptive warping, seam cutting, and deep image stitching aim to seamlessly merge two input images, with visual quality as the primary criterion. However, they generally overlook whether the stitched result preserves the underlying 3D projection geometry while this geometric consistency is critical for enabling downstream 3D vision tasks such as structure-from-motion, SLAM, visual pose estimation, and depth estimation.

In summary, if we can stitch images with very large parallax and produce not only visually seamless result but also are capable to support downstream 3DV tasks.

1.2 Contribution

As shown in Fig. 2, to tackle the challenges of existing methods in handling extreme parallax, we introduce a novel image stitching framework named **PIS3R**, which leverages deep 3D reconstruction to achieve robust alignment under very large parallax conditions. Our method begins by applying a feed-forward scene reconstruction approach VGGT (Wang et al. 2025) to a pair of uncalibrated input images, recovering both intrinsic and extrinsic camera parameters along with a dense 3D reconstruction of the scene. The resulting point cloud is then reprojected onto a designated reference view using the estimated camera poses, yielding an initial stitched image with pixel-wise geometric alignment. To further refine this result and mitigate artifacts such as holes or noise introduced during reprojection, we incorporate a point-conditioned image diffusion module.

Unlike existing approaches that primarily focus on visual seamlessness, our method explicitly preserves the 3D

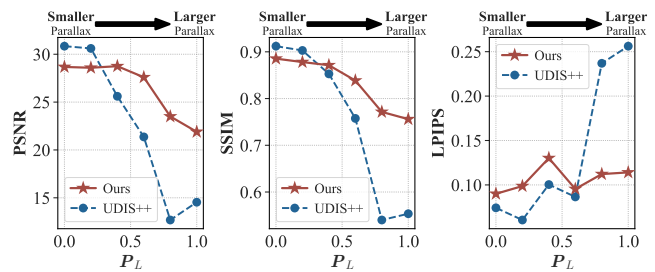


Figure 2: The relationship between quality of stitched image and parallax variation. Our PIS3R method maintains significantly higher stability than UDIS++ across all three metrics (PSNR, SSIM, and LPIPS). As Parallax level P_L (Sec. B, Appendix) increases, stitched image quality from UDIS++ degrades substantially, whereas PIS3R demonstrates superior robustness to parallax variations. Moreover, PIS3R delivers comparable visual quality to state-of-the-art methods under pure rotation and slight parallax.

geometric consistency of every pixel in the photogrammetric space. This not only enables high-quality stitching under large parallax but also ensures compatibility with downstream 3D vision tasks such as SfM, SLAM, and depth estimation. Experimental results confirm that PIS3R outperforms both qualitatively and quantitatively compared to existing methods. Our contributions center around:

- We propose a novel pipeline for stitching images with very large parallax based on the deep 3D reconstruction results and followed by a diffusion-based refinement, called PIS3R, which is a fundamental departure from the technical pipeline of existing methods.
- The idea of applying deep 3D reconstruction for image stitching that allows the produced results to achieve not only visually seamless alignment but also maintain 3D projection consistency, which enables our method to better support downstream 3D tasks such as SfM and SLAM over SOTAs.

2 Related Work

Traditional image stitching. 1) *Adaptive warping.* Traditional stitching methods often leverage discriminative features like SIFT (Lowe 2004) for estimating flexible warps such as DHW (Gao, Kim, and Brown 2011), APAP (Zaragoza et al. 2014), and TFA (Lin et al. 2011). Extensions like DFW (Li et al. 2017) and GES-GSP (Lin et al. 2021a) incorporate lines, edges, or semantic planes to enhance structural preservation. Furthermore, depth and planar priors have been utilized to improve alignment under challenging conditions (Liu et al. 2020; Zhou et al. 2018). 2) *Seam cutting.* Seam-cutting is commonly employed as a post-processing step for artifact reduction. Methods define energy terms based on photometric, gradient, or motion cues (Kwatra et al. 2003; Agarwala et al. 2004; Bao, Sun, and Yang 2013), and minimize them via graph cuts to produce visually coherent results. Seam-based alignment optimization has also been explored for minimizing stitching distortions (Zhang and Liu 2014; Lin et al. 2016; Zhou, Zhang,

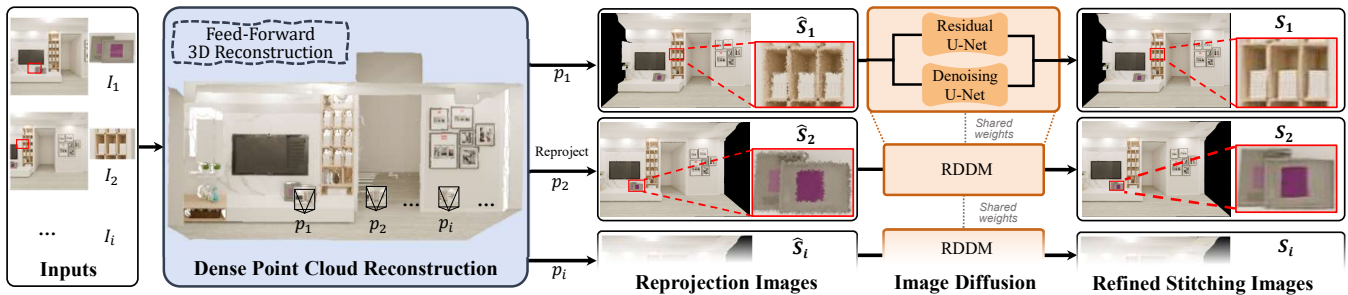


Figure 3: Overview of the PIS3R pipeline. Given a sparse image sets, we first construct a dense point cloud representation P_w using a feed-forward deep 3D reconstruction model. Subsequently, the point cloud is reprojected onto the input camera poses p_i to generate preliminary stitching images \hat{S}_i . While these images preserve the majority of the scene’s structural information, they concurrently introduce substantial noise artifacts. To address this limitation, we train a point-conditioned denoising diffusion model to restore image fidelity, ultimately producing refined stitching images S_i .

and Bao 2018). **However**, these geometry-driven methods face two limitations: 1) they are sensitive to missing or weak structural features, leading to alignment failure; and 2) when geometric features are abundant, the computational overhead increases significantly.

Deep image stitching. These approaches learn high-level semantic representations from data. They have been developed under supervised (Nie et al. 2023; Lin et al. 2021b; Zhou, Zhang, and Bao 2022; Huang, Wang, and Fu 2021; Zhou et al. 2022), weakly supervised (Nie, Zhang, and Fang 2022), and unsupervised paradigms (Nie, Zhang, and Fang 2021), demonstrating strong adaptability to complex scenes. Among these, unsupervised methods are particularly appealing due to the scarcity of ground truth stitched images. **However**, most of them rely on homography-based alignment, which struggles under very large parallax as shown in Fig. 2, often resulting in visible blur and artifacts in the reconstructed regions without mentioning being unable to preserve the 3D projection consistency.

3 Methodology

In this section, we start with a introduction to our image stitching framework(PIS3R). Subsequently, we provide a detailed explanation of the proposed framework and its components. Finally, we present our implementation details.

3.1 PIS3R Pipeline

Fig. 3 illustrates the overall architecture of our PIS3R framework. PIS3R is composed of three components as follows:

Step 1: 3D reconstruction. Given a sparse set of two or more images, we first establish their point cloud representation using a dense stereo model, as illustrated in Sec. 3.2.

Step 2: Point Cloud Reprojection. Subsequently, we reproject the point cloud onto the input camera poses predicted by the dense stereo model to obtain a preliminary stitched image, as illustrated in Sec. 3.3.

Step 3: Refinement of Reprojected Images. To achieve visually pleasing results while preserving the geometric structure of the scene, we train a point-conditioned image diffusion model to refine the noisy preliminary stitched image, as depicted in Sec. 3.4.

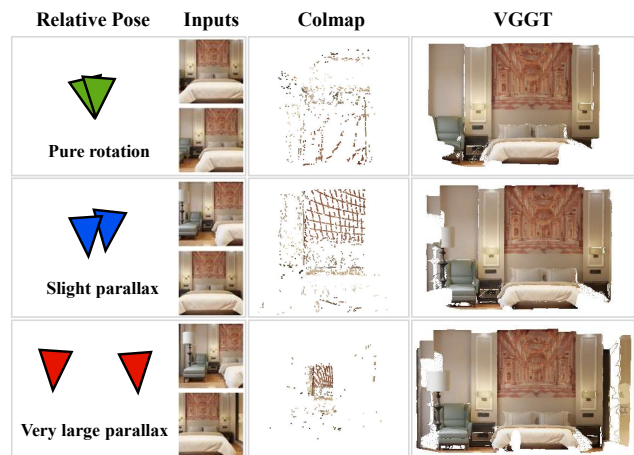


Figure 4: Visual Comparison of 3D Reconstruction Results between COLMAP and VGGT. Reconstruction is performed under three distinct camera pose scenarios: pure rotation, slight parallax, and very large parallax. It can be observed that COLMAP produces significantly sparser point clouds across all scenarios, capturing limited structural information. In contrast, VGGT generates dense point clouds that preserve the majority of scene details.

3.2 Deep-based 3D Reconstruction

As shown in Fig. 3, we first construct a point cloud representation from the input images to obtain information about the entire scene. Certainly different from prior approaches that achieve image stitching through geometry-based 3D reconstruction, we adopts a deep-based reconstruction framework. Specifically, we employ **VGGT** (Wang et al. 2025)¹ to reconstruct the entire scene and estimate camera parameters simultaneously. The input consists of a sequence of RGB images capturing the same 3D scene $(I_i)_{i=1}^N \in \mathbb{R}^{H \times W \times 3}$ to corresponding 3D annotation information via a transformer,

¹<https://github.com/facebookresearch/vggg>

which can be described as:

$$F \left((I_i)_{i=1}^N \right) = (\mathbf{g}_i, D_i, P_i, E_i)_{i=1}^N, \quad (1)$$

where $\mathbf{g}_i \in \mathbb{R}^9$ is the camera intrinsic and extrinsic parameters, its depth map $D_i \in \mathbb{R}^{H \times W}$ and point map $P_i \in \mathbb{R}^{3 \times H \times W}$ and a grid $E_i \in \mathbb{R}^{C \times H \times W}$.

As shown in Fig. 4, we compare the point cloud representations generated by the geometry-based reconstruction framework COLMAP (Schönberger et al. 2016; Schönberger and Frahm 2016)² and VGGT under three different input settings: pure rotation, slight parallax, and very large parallax. The reconstruction performance of COLMAP under sparse viewpoints is predictable, while the reconstruction results of VGGT are remarkable. The quality of the point cloud and the accuracy of the predicted camera poses are crucial for image stitching using 3D reconstruction. This directly determines the geometric structure and quality of final stitched image.

3.3 Image Stitching via Point Cloud Reprojection

As shown in Fig. 3, to obtain the reprojected image \hat{S}_i from I_i , we first generate the transformed point cloud $P_c^i \in \mathbb{R}^{NHW \times 3}$ by converting the predicted point cloud $P_w \in \mathbb{R}^{NHW \times 3}$ from the world coordinate to the camera coordinate O_c^i using the camera extrinsic parameters (rotation R^i and translation t^i). The transformation from world coordinates to camera coordinates can be described as:

$$P_c^i = R^i P_w + t^i, \quad (2)$$

where $R^i \in \mathbb{R}^{3 \times 3}$ is the rotation matrix and $t^i \in \mathbb{R}^3$ is the translation vector for camera i . Subsequently, we reproject P_c^i onto the pixel coordinates O_{uv}^i , resulting in the pixel-wise projected points P_{uv}^i according to Eq. 3:

$$P_{uv}^i = \frac{K_i P_c^i}{Z}, \quad (3)$$

where K_i is the intrinsic matrix of camera i , and Z denotes the depth of each 3D point in P_c^i . Finally, the reprojected image \hat{S}_i is constructed by normalizing the pixel values at the reprojected positions according to Eq. 4:

$$\hat{S}_i = \text{Normalize}(P_{uv}^i), \quad (4)$$

where $\text{Normalize}(\cdot)$ denotes normalize the reprojected pixel values to the non-negative coordinate space.

We integrate the point map with its corresponding RGB image to obtain the reprojected image at the respective pose. This provides coarse 3D scene information for image stitching. However, sparse inputs offer insufficient 3D cues, which cause significant missing regions, occlusions, and artifacts in the reconstructed point cloud. These issues further cause missing regions and pixel misalignments in the reprojected images. Therefore, we propose integrating image diffusion models to obtain visually pleasing stitched image.

²<https://github.com/colmap/colmap>

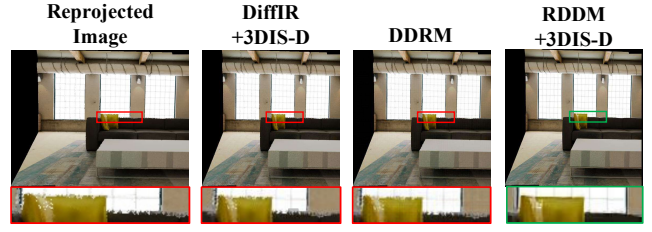


Figure 5: Qualitative comparison of different image restoration diffusion models. We evaluated the performance of several state-of-the-art image restoration diffusion models in refining reprojected images, including DiffIR (Xia et al. 2023), DDRM (Kawar et al. 2022), and RDDM (Liu et al. 2024).

3.4 Diffusion-based Stitching Refinement

As illustrated in Fig. 3, to improve the quality of the reprojected image, our goal is to learn a conditional distribution $x \sim p(x|\hat{S})$ that generates high-quality image from the degraded reprojected image. As shown in Fig. 5 and Sec. 5.4, we compared three image restoration diffusion models. Specifically, we employ **RDDM** (Liu et al. 2024) modifies to refine reprojected image \hat{S} . Different from traditional diffusion model, RDDM extends $x_T = \varepsilon$ to $x_T = x_{in} + \varepsilon$ and changes the forward diffusion process by incorporating a mixture of three terms (i.e., x_0 , x_{res} , and ε):

$$x_t = x_{t-1} + \alpha_t x_{res} + \beta_t \varepsilon_{t-1}, \quad (5)$$

$$x_t = x_0 + \bar{\alpha}_t x_{res} + \bar{\beta}_t \varepsilon_t, \quad (6)$$

where α_t and β_t are coefficients that respectively control the residual and noise injection, $\bar{\alpha}_t = \sum_{i=1}^t \alpha_i$, $\bar{\beta}_t = \sqrt{\sum_{i=1}^t \beta_i^2}$, $x_{res} = x_{in} - x_0$, and $\varepsilon \sim \mathcal{N}(0, I)$.

The reverse process can be formulated as $p_\theta(x_{t-1}|x_t) := q_\sigma(x_{t-1}|x_t, x_0^\theta, x_{res}^\theta)$, where x_0^θ , x_{res}^θ are respectively predicted by a residual U-Net and a denoising U-Net. And estimated target image $x_0^\theta = x_t - \bar{\alpha}_t x_{res}^\theta - \bar{\beta}_t \varepsilon_\theta$ can be recovered according to Eq. 6. Subsequently, residual U-Net and denoising U-Net are optimized by the diffusion loss:

$$\min_{res(\theta)} = \mathbb{E} \left[\lambda_{res} \|x_{res} - x_{res}^\theta(x_t, t, x_{in})\|^2 \right], \quad (7)$$

$$\min_{\varepsilon(\theta)} = \mathbb{E} \left[\lambda_\varepsilon \|\varepsilon - \varepsilon_\theta(x_t, t, x_{in})\|^2 \right] \quad (8)$$

RDDM begins with residual information that captures the differences between the target and degraded images. Thus, it can effectively guide the restoration process, maximally preserve the original 3D information provided by the reprojected image, and better maintain the consistency of the geometric structure.

3.5 Implementation

• **3D reconstruction.** We directly use the opensource pre-trained model of VGGT to complete 3D reconstruction. To ensure the integrity of the scene information, we accept all predicted points without applying a confidence threshold.

- **Diffusion model.** To train the RDDM model, we created paired training data consisting of degraded and corresponding ground truth images. To better suit our task, we manually processed ground truth images from the **RainDrop** dataset (Qian et al. 2018) to generate the customized 3DIS-D dataset, incorporating various noises for enhanced robustness beyond reprojection artifacts and occlusions.

We adopted a progressive training strategy with a global learning rate of $8e^{-5}$ and batch size of 1. In the first stage, we trained on 3DIS-D at 512×512 resolution with 10 sampling steps for 120,000 iterations, using ground truth as targets and processed images as degraded inputs. In the second stage, we fine-tuned on **GoPro** (Nah, Hyun Kim, and Mu Lee 2017) dataset at the same resolution with 5 sampling steps for 20,000 iterations. Notably, our approach achieves satisfactory results with limited training data. All training and testing were performed on an NVIDIA RTX 4090 GPU.

4 Discussion

- **Is PIS3R suitable for pure rotation or slight parallax?** PIS3R delivers comparable visual quality to state-of-the-art methods under pure rotation or slight parallax (Fig. 3, Appendix) but requires more processing time per image than UDIS++ (Tab. 1, Appendix). We recommend PIS3R for scenarios with large parallax and propose a parallax classifier (Sec. B, Appendix) to estimate input image parallax levels.

- **Why deep 3DR?** Deep 3DR solutions such as VGGT demonstrate significantly greater robustness and accuracy than classical SfM like COLMAP in estimating camera intrinsic and extrinsic parameters, particularly in challenging two-view scenarios such as pure rotation and very large parallax (as shown in Fig. 1 and detailed in the Sup material). Moreover, the point maps predicted by VGGT offer substantially higher density compared to traditional SfM point clouds, providing strong support for the following image stitching reprojection step.

- **Why PIS3R is geometry-preserve?** PIS3R employs a deep-based reconstruction framework to accurately predict the point cloud representation and the camera intrinsic and extrinsic parameters. Accurate pose estimation of the images is fundamental to preserving geometric structure in PIS3R. This is also the reason why SOTA methods fail to maintain geometric structure. As illustrated in Sec. 5.3 and tab. 2.

- **How does PIS3R support 3D vision downstream tasks?** Our preliminary stitched image is generated via reprojection based on the camera parameters. This provides the stitched image with accurate geometric spatial information. As shown in Fig. 6 and Sec. 5.3, stitching results of PIS3R in very large parallax scenarios can be directly input into a geometry-based 3D reconstruction framework for point cloud reconstruction, while better maintaining the geometric structure and integrity of the scene due to its excellent geometry preservation capability.

- **Limitation?** PIS3R, while effective in many scenarios, is not without limitations. As with most SOTA image stitching approaches, certain constraints must be acknowledged:

- **Extremely large parallax and rotation:** When both large parallax and considerable rotation are present in the

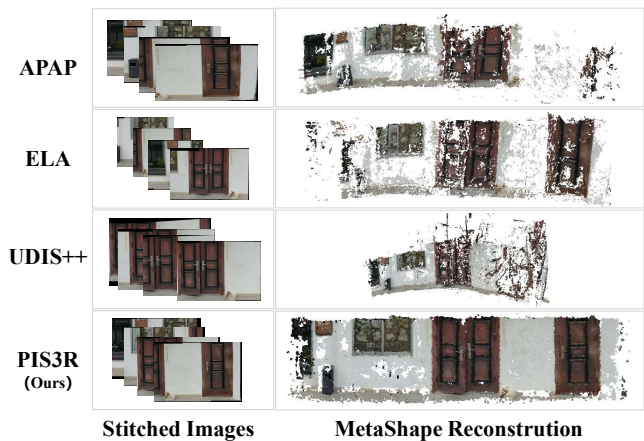


Figure 6: The results of MetaShape reconstruction using stitched images. When used as inputs for 3D reconstruction in MetaShape, images stitched with APAP and ELA resulted in large number of surface holes. Images stitched with UDIS++ exhibited significant distortions to geometric structure. In contrast, reconstructions generated from our stitched images consistently exhibited high geometric consistency and completeness within MetaShape. This enhanced structural integrity suggests that PIS3R is more suitable for downstream 3D reconstruction tasks.

input images, non-overlapping areas in either the foreground or background during the reprojection process may lead to pronounced missing regions and distortions.

- **Large-area object occlusion:** When the occluded area of the background is large, the missing regions in the reprojected image lack detailed geometric structure. This effectively disables the residual diffusion process in those areas, leading to pure noise generation, which results in distortions, inconsistencies, and holes.

5 Experiments

In this section, we conduct a comprehensive series of comparative experiments to evaluate the performance of our method PIS3R. We compare PIS3R against three state-of-the-art image stitching solutions: **APAP** (Zaragoza et al. 2014), **ELA** (Li et al. 2018) and **UDIS++** (Nie et al. 2023).

5.1 Datasets

- **Synthetic Dataset:** As shown in Fig. 8a, this test dataset was rendered using Blender. It comprises 20 distinct scenes^{3 4 5} with 600 image pairs and their corresponding ground truth (GT) images. Most image pairs have large-baseline, large-parallax characteristics.

- **Real-World Dataset:** As shown in Fig. 8b, we capture the dataset with a mobile phone. It comprises 10 distinct scenes with 682 image pairs and their corresponding GT images.

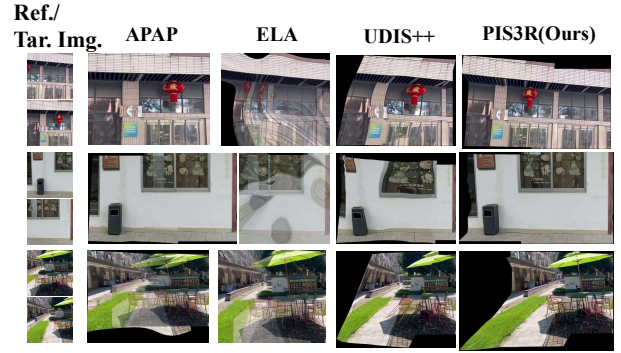
³<https://sketchfab.com>

⁴<https://blenderco.cn/>

⁵<https://free3d.com/zh/3d-models/blender>



(a) Qualitative comparison of stitched images on synthetic dataset.



(b) Qualitative comparison of stitched images on real-world dataset

Figure 7: Qualitative comparison of stitched images on synthetic dataset and real-world dataset. Our PIS3R generates images with significantly more complete structures and fewer severe distortions compared to existing image stitching algorithms APAP, ELA and UDIS++ in both datasets. Ref./Tar. Img. refers to Reference and Target Images.

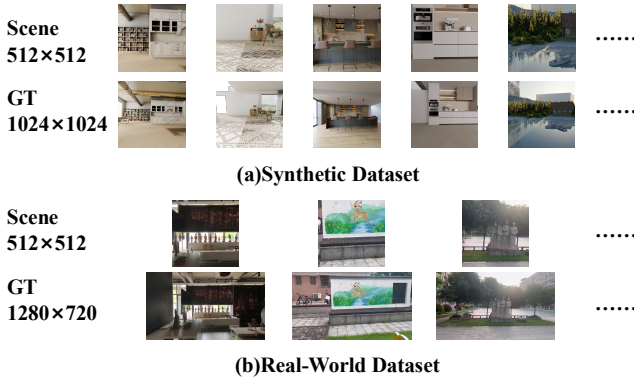


Figure 8: Sample images from the experimental dataset. (a) Synthetic dataset rendered by Blender (Community 2018). (b) Real-world dataset captured by ourselves. Additionally, each scene image and its ground-truth image share the same camera extrinsics.

We test this real-world dataset to validate the performance of PIS3R in real-world scenarios.

5.2 Comparison of Image Stitching

Evaluation Metrics. The traditional image stitching paradigm consists of warping and composition stages. However, as a 3D-reconstruction-based image stitching paradigm, PIS3R does not include these steps. Therefore, overlapping regions based metrics of warping results is not suitable for PIS3R. Notably, each reference image shares the same camera extrinsics with its GT image (Fig. 8), and scene images are obtained by center-cropping GT images. Theoretically, stitched images should share the same extrinsics with reference images. Thus, we propose a novel three-step metric computation approach (Fig.4 in Appendix):

Step 1: Padding. Firstly, we pad the reference image to match the size of the GT image.

Step 2: Registration. Subsequently, we register the stitched image to the padded reference image.

Step 3: Compute metrics. Then we can compute metrics for the valid pixels between the registered stitched image and the GT image.

We employ metrics including: **PSNR**, **SSIM** (Wang et al. 2004), **LPIPS** (Zhang et al. 2018). Furthermore, to avoid metric inaccuracies caused by registration failures, we calculated the Registration Success Rate (**RSR**):

$$RSR = (1 - \frac{R_f}{n}) \times 100\%, \quad (9)$$

where n is the total image pairs in dataset, R_f is the number of failed registration cases. Subsequently, we recomputed the metrics excluding the registration failed cases.

Image Stitching in Synthetic Dataset. We first evaluate four different methods on our custom synthetic dataset.

• **Qualitative Comparison.** The qualitative comparison results are shown in Fig. 7a, where the reference and target images are displayed in the left-most column. APAP, ELA and UDIS++ exhibit noticeable artifacts and geometric inconsistencies, while Our results better preserve the geometric structure of the scene. Additional cases are provided in Fig. 1 of Appendix.

• **Quantitative Comparison.** The quantitative comparison results are presented in Tab. 1. Our PIS3R outperforms the other three methods across all metrics when including all data in the calculations. We still maintain a substantial lead in PSNR, SSIM after excluding failed registration cases. What is noteworthy is that **RSR** substantially indicates the method’s ability to maintain geometric consistency.

Image Stitching in Real-World Dataset. We employ a real-world dataset captured by ourselves to validate the performance of PIS3R in real-world scenarios.

• **Qualitative Comparison.** The qualitative comparison results are presented in Fig. 7b. APAP, ELA and UDIS++ exhibit noticeable artifacts and geometric inconsistencies. In contrast, our PIS3R method consistently generates images with significantly more complete structures and fewer severe distortions in these complex and challenging scenarios. Additional cases are provided in Fig. 2 of Appendix.

Dataset	Method	All Image Pairs				W/O Failed Registration Cases		
		PSNR \uparrow	SSIM \uparrow	LPIPS \downarrow	RSR \uparrow	PSNR \uparrow	SSIM \uparrow	LPIPS \downarrow
Synthetic Dataset	APAP	19.116	0.659	0.169	87.5%	20.063	0.691	0.146
	ELA	19.813	0.67	0.158	91.5%	20.487	0.719	0.139
	UDIS++	19.858	0.690	0.139	86.2%	21.038	0.748	0.097
	PIS3R	22.026	0.782	0.110	95.7%	22.351	0.796	0.102
Real World Dataset	APAP	16.764	0.525	0.246	81.6%	18.047	0.572	0.207
	ELA	16.983	0.547	0.245	98.2%	17.064	0.553	0.242
	UDIS++	17.390	0.554	0.204	90.3%	18.874	0.615	0.208
	PIS3R	19.674	0.644	0.180	100.0%	19.674	0.644	0.180

Table 1: Quantitative comparison of image stitching on synthetic dataset and real world dataset. PIS3R outperforms the other three methods across PSNR, SSIM and LPIPS when all image pairs are included in the evaluation. Moreover, even after excluding registration-failed cases, PIS3R still maintains a noticeable advantage in PSNR and SSIM.

- **Quantitative Comparison.** As shown in Tab. 1, PIS3R demonstrates superior performance across all evaluation metrics on the complete real-world dataset. Moreover, after excluding failed registration cases, it continues to achieve leading performance on all metrics.

5.3 Geometric Consistency Verification of Stitched Images

In this section, we perform geometric consistency verification on stitched images of synthetic dataset to ensure structural accuracy.

- **Evaluation Metric.** Since the camera parameters of the images in Blender are available, we evaluated Geometric Consistency by computing the Sampson Epipolar Error (d_{sam}^2) on two stitched images:

$$d_{sam}^2 = \frac{(x_2^\top F x_1)^2}{(F x_1)_1^2 + (F x_1)_2^2 + (F^\top x_2)_1^2 + (F^\top x_2)_2^2}, \quad (10)$$

where F is fundamental matrix, x_1 and x_2 respectively denote the homogeneous coordinates of a pair of corresponding feature points detected in the first and second images.

- **Qualitative Comparison.** As shown in Fig. 6, we fed the stitched images of each method into Agisoft MetaShape (Agisoft LLC 2023) for reconstruction. PIS3R’s stitching results in very large parallax scenarios can be directly input into a Structure From Motion (sfm) framework for point cloud reconstruction, while better maintaining the geometric structure and integrity of the scene due to its excellent geometry preservation capability.

- **Quantitative Comparison.** As shown in Table 2, PIS3R achieves a significantly lower epipolar error for stitched images exhibiting very large parallax conditions, notably outperforming the other three approaches.

	APAP	ELA	UDIS++	PIS3R
d_{sam}^2 (pixel) \downarrow	22.78	38.97	12.94	4.12

Table 2: Sampson epipolar error of stitching image on synthetic dataset. PIS3R achieves a lower epipolar error for stitched images exhibiting very large parallax conditions.

5.4 Ablation studies

Comparison of Different Diffusion Models. As shown in Fig. 5, we compared three image restoration diffusion models: DiffIR (Xia et al. 2023)⁶, DDRM (Kawar et al. 2022)⁷, and RDDM (Liu et al. 2024)⁸. We train DiffIR and RDDM on 3DIS-D dataset (as illustrated in Sec. 3.5) and present comparative results of the restoration performance. Notably, DDRM does not rely on task-specific training and can be applied directly. RDDM can effectively remove noise while preserving geometric structures.

Quantitative Impact of Diffusion Models. We quantify the metric differences between reprojected images processed and unprocessed by the diffusion model. As shown in Tab. 2, 3 in Appendix, diffusion model notably enhances stitched images’ visual quality while having a negligible impact on the evaluation metrics. This trade-off is thus deemed both acceptable and necessary.

6 Conclusion

We proposed PIS3R, a very large parallax-tolerant image stitching framework based on deep 3D reconstruction. By estimating camera parameters and reconstructing a dense point cloud via a visual geometry-grounded transformer, our method achieves pixel-wise alignment through reprojection. A point-conditioned image diffusion module further refines the result. Unlike existing methods, PIS3R preserves 3D geometric consistency, enabling seamless stitching and compatibility with downstream 3D tasks. Experimental results show that PIS3R outperforms prior approaches both visually and quantitatively under very large parallax.

References

Agarwala, A.; Agrawala, M.; Cohen, M.; Curless, B.; Salesin, D.; and Szeliski, R. 2004. Interactive digital photomontage. In *ACM Transactions on Graphics (TOG)*, volume 23, 294–302.

⁶<https://github.com/Zj-BinXia/DiffIR>

⁷<https://github.com/bahjat-kawar/ddrm>

⁸<https://github.com/nachifur/RDDM>

- Agisoft LLC. 2023. Agisoft Metashape - Professional Photogrammetry Software. <https://www.agisoft.com/>. Accessed: [2025-1-15].
- Bao, L.; Sun, J.; and Yang, Q. 2013. Fast edge-preserving patchmatch for large displacement optical flow. *IEEE Transactions on Image Processing*, 22(12): 5004–5017.
- Community, B. O. 2018. *Blender - a 3D modelling and rendering package*. Blender Foundation, Stichting Blender Foundation, Amsterdam.
- Gao, J.; Kim, S.; and Brown, M. S. 2011. Constructing image panoramas using dual-homography warping. In *CVPR*, 49–56.
- Gao, J.; Li, Y.; Chin, T.-J.; and Brown, M. S. 2013. Seam-driven image stitching. In *Proceedings of the Eurographics (EG)*.
- Hartley, R.; and Zisserman, A. 2003. *Multiple View Geometry in Computer Vision*. Cambridge University Press.
- Huang, W.; Wang, K.; and Fu, J. 2021. Image stitching with transformer. In *ACCV*.
- Kawar, B.; Elad, M.; Ermon, S.; and Song, J. 2022. Denoising diffusion restoration models. *Advances in neural information processing systems*, 35: 23593–23606.
- Kwatra, V.; Schodl, A.; Essa, I.; Turk, G.; and Bobick, A. 2003. Graphcut textures: Image and video synthesis using graph cuts. In *SIGGRAPH*, 277–286.
- Lee, K.-Y.; and Sim, J.-Y. 2018. Stitching for multi-view videos with large parallax based on adaptive pixel warping. *IEEE Access*, 6: 26904–26917.
- Li, J.; Wang, Z.; Lai, S.-H.; Zhai, Y.; and Zhang, M. 2018. Parallax-tolerant image stitching based on robust elastic warping. *IEEE Transactions on Multimedia*, 20(7): 1672–1687.
- Li, X.; Zhao, Y.; Lu, H.; and Wang, R. 2017. Dual-feature warping based robust image stitching. In *ICIP*, 2394–2398.
- Lin, K.; Jiang, N.; Cheong, L.-F.; Do, M. N.; and Lu, J. 2016. Seagull: Seam-guided local alignment for parallax-tolerant image stitching. In *ECCV*, 370–385.
- Lin, K.; Lu, J.; Zhou, J.; and Zheng, Z. 2021a. GES-GSP: Geometrically and Semantically consistent image stitching via grid-based spatial partitioning. *IEEE Transactions on Image Processing*, 30: 2115–2128.
- Lin, W.; Liu, S.; Matsushita, Y.; Ng, T.-T.; and Cheong, L.-F. 2011. Smoothly varying affine stitching. In *CVPR*, 345–352.
- Lin, Z.; Xu, X.; Liu, Z.; and Wei, W. 2021b. Deep image stitching via exploring semantic cues. In *ACM Multimedia*, 1234–1242.
- Liu, J.; Wang, Q.; Fan, H.; Wang, Y.; Tang, Y.; and Qu, L. 2024. Residual denoising diffusion models. In *Proceedings of the IEEE/CVF Conference on Computer Vision and Pattern Recognition*, 2773–2783.
- Liu, Y.; Yang, J.; Zhu, T.; Fu, J.; and Luo, J. 2020. Attentional semantic alignment for panorama image stitching. In *ECCV*, 128–144.
- Lowe, D. G. 2004. Distinctive image features from scale-invariant keypoints. *International journal of computer vision*, 60(2): 91–110.
- Nah, S.; Hyun Kim, T.; and Mu Lee, K. 2017. Deep multi-scale convolutional neural network for dynamic scene deblurring. In *Proceedings of the IEEE conference on computer vision and pattern recognition*, 3883–3891.
- Nie, W.; Zhang, Y.; and Fang, Y. 2021. Unsupervised Deep Homography for Parallax-Robust Image Stitching. In *ICIP*, 3153–3157.
- Nie, W.; Zhang, Y.; and Fang, Y. 2022. Unsupervised image stitching with deep homography alignment and local refinement. In *Proceedings of the IEEE International Conference on Multimedia and Expo (ICME)*.
- Nie, W.; Zhang, Y.; Zhu, J.; Wang, Y.; Chen, Y.; and Fang, Y. 2023. Parallax-Tolerant Unsupervised Deep Image Stitching. In *Proceedings of the IEEE/CVF International Conference on Computer Vision (ICCV)*.
- Qian, R.; Tan, R. T.; Yang, W.; Su, J.; and Liu, J. 2018. Attentive generative adversarial network for raindrop removal from a single image. In *Proceedings of the IEEE conference on computer vision and pattern recognition*, 2482–2491.
- Schönberger, J. L.; and Frahm, J.-M. 2016. Structure-from-Motion Revisited. In *Conference on Computer Vision and Pattern Recognition (CVPR)*.
- Schönberger, J. L.; Zheng, E.; Pollefeys, M.; and Frahm, J.-M. 2016. Pixelwise View Selection for Unstructured Multi-View Stereo. In *European Conference on Computer Vision (ECCV)*.
- Wang, J.; Chen, M.; Karaev, N.; Vedaldi, A.; Rupprecht, C.; and Novotny, D. 2025. Vggt: Visual geometry grounded transformer. In *Proceedings of the Computer Vision and Pattern Recognition Conference*, 5294–5306.
- Wang, Z.; Bovik, A. C.; Sheikh, H. R.; and Simoncelli, E. P. 2004. Image quality assessment: from error visibility to structural similarity. *IEEE transactions on image processing*, 13(4): 600–612.
- Xia, B.; Zhang, Y.; Wang, S.; Wang, Y.; Wu, X.; Tian, Y.; Yang, W.; and Van Gool, L. 2023. Diffir: Efficient diffusion model for image restoration. In *Proceedings of the IEEE/CVF international conference on computer vision*, 13095–13105.
- Zaragoza, J.; Chin, T.-J.; Tran, Q.-H.; Brown, M. S.; and Suter, D. 2014. As-projective-as-possible image stitching with moving DLT. *TPAMI*, 36(7): 1285–1298.
- Zhang, F.; and Liu, F. 2014. Parallax-tolerant image stitching. In *CVPR*, 3262–3269.
- Zhang, G.; He, Y.; Chen, W.; Jia, J.; and Bao, H. 2016. Multi-viewpoint panorama construction with wide-baseline images. *IEEE Transactions on Image Processing*, 25(7): 3099–3111.
- Zhang, R.; Isola, P.; Efros, A. A.; Shechtman, E.; and Wang, O. 2018. The unreasonable effectiveness of deep features as a perceptual metric. In *Proceedings of the IEEE conference on computer vision and pattern recognition*, 586–595.
- Zhou, T.; Liu, M.; Zhang, G.; and Bao, H. 2022. WarpStitch: Learning topology-aware warping for image stitching. In *ECCV*, 670–687.

- Zhou, T.; Zhang, G.; and Bao, H. 2018. Stitchability determination for image stitching. In *ECCV*, 162–177.
- Zhou, T.; Zhang, G.; and Bao, H. 2022. Learning multi-homography alignment with attention for panoramic image stitching. In *CVPR*, 1324–1333.
- Zhou, T.; Zhang, X.; Bao, H.; and Zhang, G. 2018. Stereo-aware multi-projective warping for panoramic image stitching. In *ECCV*, 21–36.